Advanced Materials

ADVANCED MATERIALS
www.advmat.de

RESEARCH ARTICLE

Unlocking Wafer-Scale 3D Photonic Systems With Ion-Beam-Induced Origami

Yi Wang[1] | Ruixuan Zheng[2] | Cai Luo[1] | Ziyi Fu[1] | Nannan Hu[1] | Enbo Gao[1] | Gaojing Liu[1] | Peng Bao[1] | Weikang Fang[1] | Aizi Jin[1] | Baoli Liu[1] | Baogang Quan[1] | Geng Li[1] | Xiaofeng Fan[3] | Sha Hu[4] | Yang Guo[1,5] | Changzhi Gu[1,5]

[1]Beijing National Laboratory For Condensed Matter Physics, Institute of Physics, Chinese Academy of Sciences, Beijing, China | [2]New Cornerstone Science Laboratory, Department of Physics, University of Hong Kong, Hong Kong, China | [3]Key Laboratory of Automobile Materials of MOE, College of Materials Science and Engineering, Jilin University, Changchun, China | [4]School of Physics and New Energy, Henan University of Technology, Zhengzhou, China | [5]School of Physical Sciences, CAS Key Laboratory of Vacuum Physics, University of Chinese Academy of Sciences, Beijing, China

Correspondence: Yang Guo (yangguo@iphy.ac.cn) | Changzhi Gu (czgu@iphy.ac.cn)

Received: 10 February 2026 | **Revised:** 14 May 2026 | **Accepted:** 15 June 2026

Keywords: fabrication | grating | materials science | nanoscopic scale | nanotechnology | optoelectronics | photonics | wafer

ABSTRACT

Scalable manufacturing of three-dimensional (3D) micro-/nano-architectures with nanometric precision remains a pivotal challenge in photonics. Here, we introduce a parallel broad-beam ion beam etching (IBE) technique that decouples this fundamental trade-off, enabling the simultaneous and uniform transformation of two-dimensional (2D) patterns into well-defined 3D geometries across entire 4-inch wafers. The IBE platform achieves angular uniformity exceeding 97% and reduces fabrication time by over two orders of magnitude compared to serial focused-ion-beam (FIB) methods. Leveraging this approach, we fabricate two distinct functional devices: a chiral 3D bending metasurface with a giant experimental circular dichroism of 0.8 in the mid-infrared, and a collectively buckled plasmonic grating whose resonance is dynamically tunable over 150 nm in the visible spectrum via curvature control. This technology uniquely combines nanoscale precision with wafer-scale throughput, enabling the construction of 3D metasurfaces via meta-atom assembly and the global modulation of optical responses. Our work establishes a versatile platform that bridges the gap between design complexity and scalable manufacturing for next-generation 3D integrated photonics.

1 | Introduction

Origami, the technique of transforming two-dimensional precursors into three-dimensional architecture, has established itself as a powerful design and manufacturing paradigm in functional micro- and nanophotonics [1–8]. By enabling the engineering of complex 3D geometries from planar templates, it provides a viable pathway to transcend the limitations of conventional 2D nanofabrication and unlock a broad range of novel optical phenomena [9–12]. This strategy not only facilitates geometric reconfiguration but also imparts materials with unprecedented functional properties, such as reconfigurability [13–15], mechanical load capacity, and multi-degree-of-freedom controllability [16–18], enabling novel optical effects [19–22]. These characteristics, which are inherently unattainable in planar systems, open promising avenues for advances in nonlinear optics [23], quantum light sources [24], and ultrasensitive molecular sensing [25–27].

Despite these prospects, the transition of 3D Origami photonics from laboratory demonstrations to practical technologies has been impeded by a fundamental fabrication constraint.

A central challenge is the lack of a manufacturing approach that concurrently satisfies the nanometric precision essential for optical functionality and the wafer-scale uniformity and throughput required for scalable production. Existing Origami methods, such as compression buckling [28–31], residual stress-induced bending [10, 32–34], capillary force origami [35–38], and electron beam induced folding [39–41], are often severely dependent on material selection and generally offer limited spatial control over the final 3D morphology, falling short of achieving the well-defined, multi-degree-of-freedom geometries necessary for high-performance photonic devices. In contrast, the method of implanting ions into lattice materials to create vacancy defects and induce tensile or compressive stress for bending is universally applicable to a wide range of materials. Moreover, ion beam irradiation enables precise control over selected meta-atoms, breaks the limitations of geometric degrees of freedom, and frees the structures from planar processing constraints and substrate clamping, thereby enabling the realization of complex 3D architectures. While focused ion beam (FIB) folding allows high-precision deformation [42–48], it is constrained by multiple factors: high instrumentation costs, resolution limits that impede reproducible fabrication of sub-wavelength features for visible-light applications, slow writing speeds, and stitching inaccuracies during large-area processing. These issues confine FIB primarily to micrometer-scale prototyping. Moreover, the directional and sequential nature of ion implantation results in non-uniform, history-dependent stress profiles, complicating the predictable fabrication of complex 3D forms.

In this work, we present a wafer-scale rapid 3D origami approach based on the IBE technique. This technique utilizes simultaneous, uniform ion irradiation across entire 4-inch substrates, directly addressing the dual bottlenecks of low throughput and structural inconsistency that have limited conventional folding methods. We first elucidate the underlying physical mechanism, where uniform ion implantation creates a deterministic stress gradient that drives parallel 3D reshaping. We then quantify the relationship between structural parameters and final geometry, demonstrating exceptional angular uniformity exceeding 97% and a reduction in fabrication time by over two orders of magnitude. To further illustrate the platform's versatility, we fabricate two functionally distinct photonic devices operating in widely separated spectral bands: a chiral 3D bending metasurface exhibiting giant circular dichroism (CD) in the mid-infrared, and a collectively buckled plasmonic grating supporting bound states in the continuum (BICs) with broadly tunable resonances across the visible spectrum.

This advanced origami technology substantially expands the application scope of origami architecture, serving not only as meta-atoms for 3D metasurface construction but also enabling global buckling modulation of optical response, thereby extending the operational range of reconfigurable photonic devices from the infrared into the visible regime. More importantly, by designing 3D meta-atoms with distinct resonance peaks and allowing their modes to overlap and couple across the spectral range, a broadband 3D chiral meta-device can be realized, offering a promising direction for the future development of 3D metasurfaces [49–51].

2 | Results

2.1 | Principle and Parallel Fabrication Characteristics of IBE

Figure 1a schematically illustrates the broad-beam IBE technique for fabricating wafer-scale 3D bending structures. The process begins with gas ionization in the ion source to form plasma, which is then accelerated through electrostatic grids to generate a collimated ion beam. This beam simultaneously irradiates the entire surface of a pre-patterned sample mounted on a multi-axis fixture, allowing precise control over irradiation angle and uniformity. Suspended silicon nitride (SiN_x) membranes serve as the primary substrate, providing not only mechanical stability and facilitating the integration of functional bilayers but also offering protection during the ion irradiation.

The transformation from 2D to 3D is driven by a deterministic stress-gradient mechanism induced by uniform ion implantation. As the collimated ion flux impinges on the sample, it creates a controlled gradient of lattice defects primarily within the near-surface region. This localized damage results in differential volumetric expansion, generating a uniform internal stress field that bends the pre-patterned bilayers in a single, parallel processing step. This intrinsic parallelism enables unprecedented throughput and macroscopic uniformity. The transition from 2D planar patterns to 3D architecture is remarkably simple, enabling direct transformation via a single processing step (Figure S1). Figure 1b shows a photograph of a fully processed 4-inch wafer, where nanostructures across the entire substrate have undergone synchronized bending with remarkable angular consistency. Figure 1c conceptualizes two distinct photonic devices fabricated simultaneously within a mere tens-of-seconds IBE cycle, demonstrating the platform's versatility and fast fabrication speed. Figure 1d shows scanning electron microscopy (SEM) images of different structures fabricated synchronously across the wafer (Figure S2), illustrating their bending configurations and demonstrating high consistency throughout.

To visualize this parallel reshaping capability, we fabricated large-scale arrays of floral and butterfly motifs on SiN_x membranes via electron-beam lithography (EBL) and dry etching, each spanning 500 × 500 μm^2. Scanning electron microscopy images acquired at 10-s intervals during a 20-s irradiation cycle document the synchronized, progressive transformation of all structures within each array from 2D to 3D in Figure 2a. The EBL exposure time for patterning these structures is approximately 6 min. Moreover, for all the structures fabricated in this work with a size of $1 \times 1\ mm^2$, the EBL exposure time does not exceed 10 min. Apart from that, this entire transformation completes within seconds, standing in stark contrast to the several hours required by FIB to pattern and irradiate an equivalent area. Specifically, FIB processing and irradiation of a 100 × 100 μm^2 region requires at least seven minutes.

The uniformity afforded by parallel processing is further highlighted using spiral architecture. As shown in Figure 2b, under broad-beam irradiation, an array of spirals covering 200 × 200 μm^2 deforms uniformly along the vertical axis, with displacement increasing consistently over time. Conversely, spirals

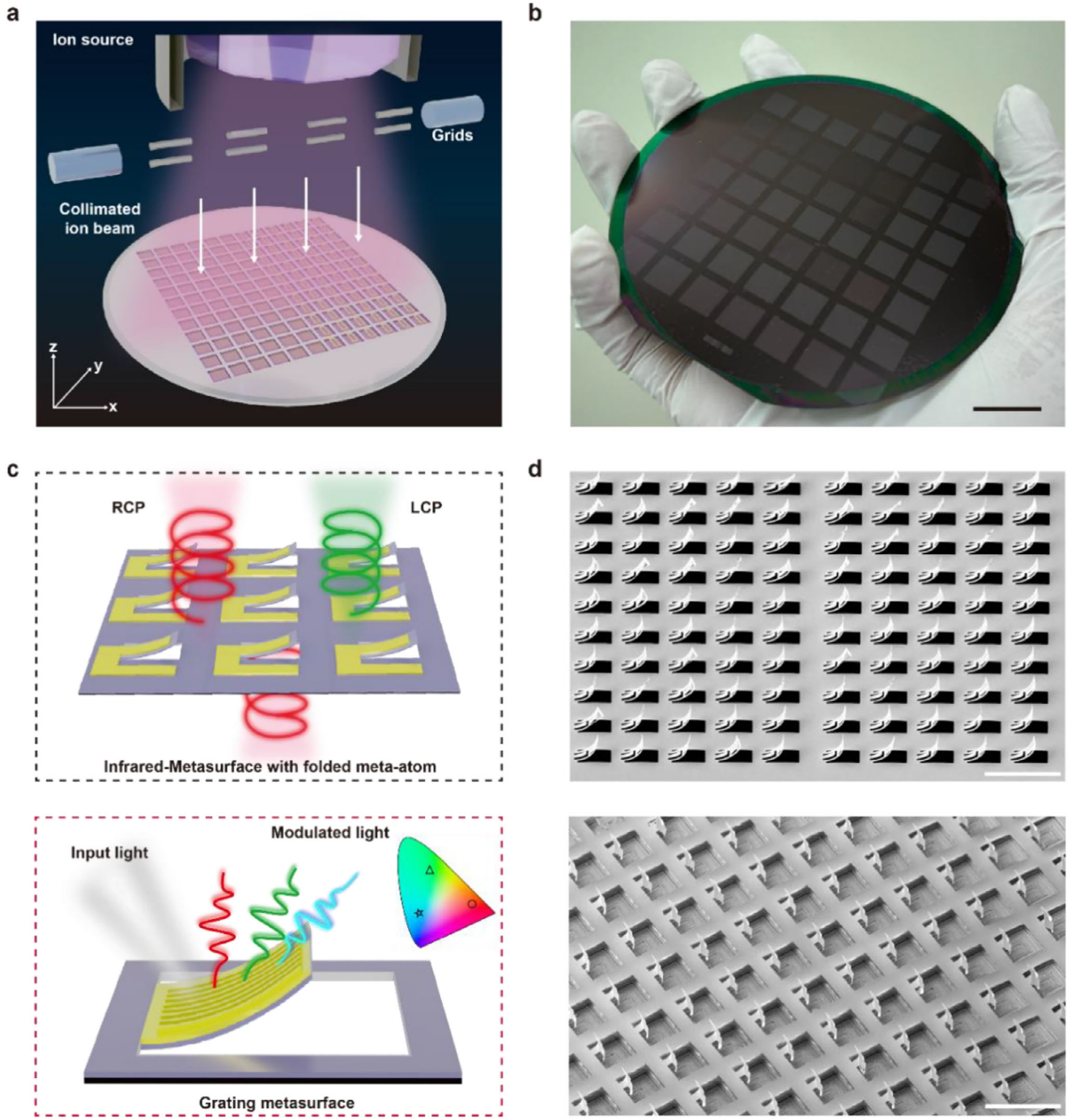

FIGURE 1 | Principle and parallel fabrication characteristics of broad-beam IBE. (a) Schematic illustration of the wafer-scale 3D origami fabrication process via broad-beam IBE. (b) Photograph of a fully processed 4-inch wafer, demonstrating uniform 3D transformation across the entire substrate. (c) Conceptual illustrations of the two distinct functional photonic devices fabricated in this work: a chiral 3D bending metasurface for mid-infrared circular dichroism (top) and a tunable collectively-buckled plasmonic grating supporting BICs for the visible spectrum (bottom). The symbols in the phase diagram mark the locations of the modulated light. (d) SEM images of other 3D fabricated structures on the wafer, with the bottom image showing the bending configuration of an η-shaped structure. Scale bars are 0.5 inch for optical images in (b), 30 μm for the top and 200 μm for the bottom image in (d), respectively.

fabricated via sequential FIB writing exhibit irregular and non-uniform reshaping. This effect becomes more pronounced with increasing dose, introducing unpredictability and complicating sample fabrication (Figure S3). This contrast stems from the fundamental difference in implantation mechanisms: IBE delivers ions uniformly and simultaneously with a low beam current density, allowing all planar structures within its irradiation range to receive the same ion flux at the same time. Consequently, they experience the same stress, leading to uniform deformation of spiral structures along the z-direction. However, in addition to injecting ions at discrete points and having a high beam current density, the processing

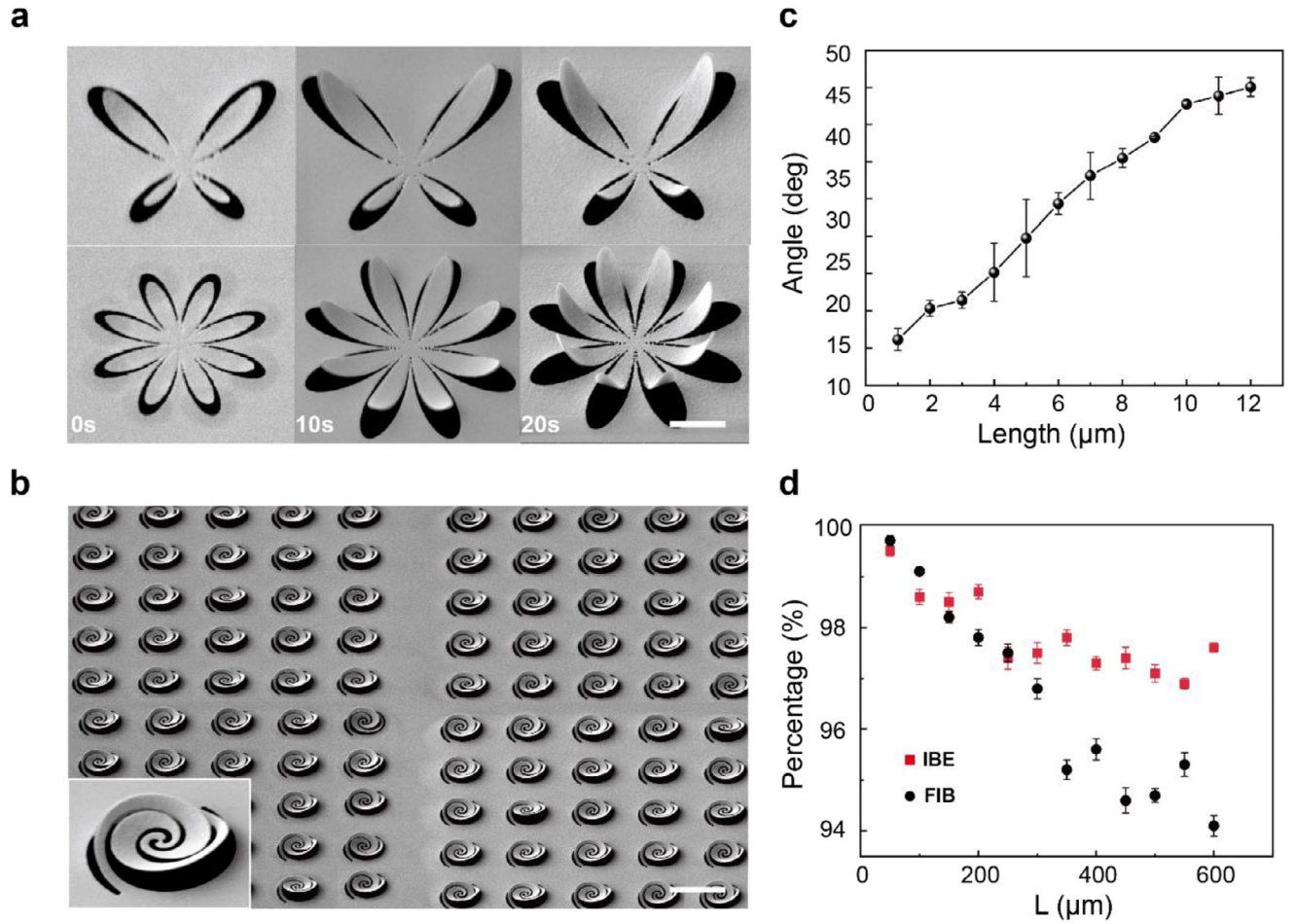

FIGURE 2 | Parallel transformation behavior and deterministic control. (a) A set of SEM images (10-s intervals) showing the synchronized, progressive 3D reshaping of floral and butterfly structures during a 20-s IBE cycle. (b) 3D SEM image of a uniformly deformed spiral array under IBE broad-beam irradiation. (c) Experimental correlation between cantilever length and bending angle α of Au/SiN_x bilayers under fixed IBE conditions, demonstrating a quasi-linear relationship and high uniformity. The thickness of both the *Au* and SiN_x layers is 50 nm. (d) Comparison of structural consistency for identical patterns processed by IBE and FIB across increasing array sizes, highlighting IBE's stable, wafer-scale performance. Scale bars are 2 μm in (a), and 20 μm in (b).

characteristics of FIB also exhibit path dependence during irradiation, whether in line-scan or area-scan mode. When the focused ion beam processes a curved spiral structure, the regions exposed first release stress and bend earlier, causing the edges to deform more than the center. This effect intensifies with increasing ion dose, making FIB-processed structures less predictable.

Precise control over the final 3D geometry is essential for functional devices. Previous studies have demonstrated that single-layer SiN_x films exhibit exclusively downward folding under ion irradiation [39]. We examined the reshaping behavior of gold-silicon nitride (Au/SiN_x) bilayer cantilevers under controlled IBE conditions. To this end, we first fabricated arrays with a variety of lengths and widths (Figure S4), each in the form of a 500 × 500 μm^2 array, to showcase the general fabrication capability. By comparing the bending behavior of cantilevers with the same length but different widths under the same irradiation time, we found that the width has little effect on the bending behavior for cantilevers with the same length (Figure S5), which can be attributed to the broad-beam irradiation nature of IBE: the number of vacancies generated by ion irradiation per unit width is the same, resulting in similar bending behavior. For quantitative analysis, arrays with a constant width of 2 μm and lengths ranging from 1 to 12 μm were selected for testing.

Following uniform irradiation, well-defined bending angles were observed with high uniformity. As shown in Figure 2c, the measured bending angle α exhibits a distinct quasi-linear dependence on cantilever length under fixed irradiation parameters (Figure S6). This relationship aligns with a basic mechanical model where the implantation-induced stress gradient remains approximately constant, leading to a curvature, and thus a bending angle, proportional to the cantilever length. Minimal data variation indicates excellent process reproducibility. We also performed Monte Carlo simulations to obtain the ion implantation depth, number of vacancies, and sputtering yield for different metal materials under ion beam irradiation. The results demonstrate that both the thickness and the nature of the metal material influence the bending curvature of the structures (Figure S7 for detailed discussion).

The mechanical response can also be tuned by adjusting the SiN_x layer thickness and the metal layer thickness, with thicker films showing a decrease in the bending curvature under identical conditions. When ions are implanted into a relatively thick material, they are densely concentrated in the surface layer, causing local volume expansion and generating compressive stress, where the stress gradient reaches its maximum. The deeper or backside layers of the material remain almost unaffected, preserving their original stress state. Due to the Bimorph effect, the expansion tendency of the surface layer is constrained by the underlying layers, ultimately converting into a macroscopic bending moment, thereby achieving bending. For the Au/SiN_x bilayer structure, a thicker SiN_x layer has a more pronounced effect on the bending curvature than a thicker gold layer. For different metal layer materials, when directly subjected to ion beam irradiation, they may exhibit different bending behaviors (e.g., *Au* and *Al*), providing an additional material-based design parameter. These trends, supported by SRIM simulations (Figure S7), establish a practical framework for predicting and controlling IBE-induced 3D deformation. Notably, the deformations in our work are plastic, forming stable 3D structures and metasurfaces without active control of the strain gradient. However, the ability to engineer strain gradients during deformation provides new possibilities for the future development of active metasurfaces.

For scalable manufacturing, preserving structural consistency with increasing area is critical. We quantified this by fabricating identical 2D patterns in arrays of varying sizes and comparing the uniformity achieved via IBE and FIB (Figure 2d). For arrays smaller than 200 × 200 μm^2, both techniques maintain high uniformity. However, as size increases, the limitations of sequential FIB processing become severe. Effects like beam drift, stage inaccuracies, and dose variations accumulate, causing rapid uniformity deterioration. In contrast, IBE-processed structures show only a modest initial uniformity decrease, which then stabilizes near 97% for arrays exceeding 500 × 500 μm^2. This stability demonstrates that IBE's uniformity is not fundamentally compromised by scale, a direct consequence of its parallel nature, establishing its authentic wafer-scale capability.

To elucidate the physical mechanism behind the ion-beam-induced bending observed at our operational energy of 300 eV, we performed Monte Carlo simulations based on the binary collision approximation. The "Stopping and Range of Ions in Matter" (SRIM) software tracks the trajectories of incident argon ions and their energy loss in the SiN_x film, which is dominated by nuclear stopping power at this low-energy regime. This results in atomic displacements and a high concentration of vacancies within a shallow surface layer in Figure 3. The key insight is that this gradient in vacancy distribution, with high concentration near the surface tapering off with depth, creates a corresponding gradient in volumetric expansion and an increase in grain boundaries, inducing a compressive stress in the irradiated layer. According to previous studies, the initial sputtering yield of SiN_x upon interaction with argon ions is known to be 0.52 (atoms/ion·eV) [52]. This non-uniform stress field generates a bending moment that drives the SiN_x film to curl toward the ion beam direction, carrying the adhered Au film along.

The simulation across a broader energy range (Figure 3) provides further support for this defect-driven stress model. It is apparent

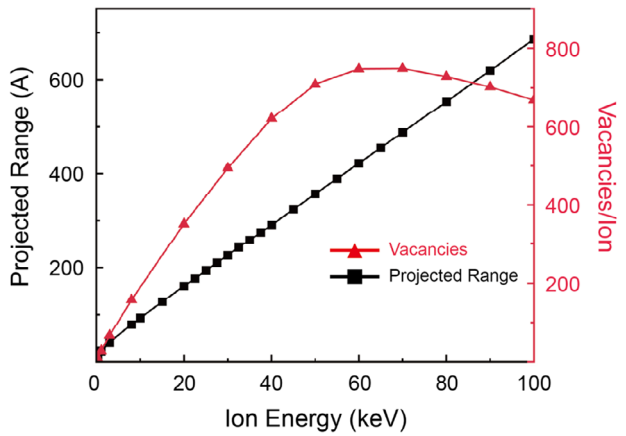

FIGURE 3 | Monte Carlo simulation results: Implantation depth and vacancy production in a 50 nm SiN_x film under argon ion implantation at varying acceleration voltages.

that the projected range has increased significantly with the increase of ion energy. The vacancy yield initially increases with ion energy as nuclear collisions intensify. As the kinetic energy increases, the energy transferred in collisions between ions and atomic nuclei also rises, resulting in a higher production of primary knock-on atoms (PKAs) and more extensive collision cascades. The subsequent decline beyond ~60 keV coincides with the transition where electronic stopping power becomes dominant. In this high-energy regime, energy is primarily dissipated through electronic excitation rather than atomic displacement, thus reducing defect production efficiency per unit path length. As shown in Figure 3, the projected range of argon ions at 300 eV is 11 A, with a corresponding vacancy number of 7.9/ Ion. This consistent physical picture across the energy confirms that the observed bending phenomenon operates unequivocally within the nuclear stopping-dominated regime, where defect-induced stress generation is most efficient.

2.2 | Fabrication and Performance of IBE-Enabled 3D Photonic Devices

Having established the parallel processing capability and deterministic reshaping behavior of the IBE platform, we demonstrate its utility by fabricating two functional 3D photonic devices. These examples leverage different aspects of IBE-induced deformation: local, sub-wavelength reshaping for creating intrinsic chirality, and global, collective buckling for enabling dynamic spectral tuning. The first is a chiral 3D bending metasurface operating in the mid-infrared, and the second is a collectively buckled grating for dynamic tuning in the visible spectrum. To achieve strong chiral selectivity in the mid-infrared, we designed a metasurface unit cell consisting of two symmetric split-ring resonators (SRRs) where one end of a designated ring is intended to be uplifted, breaking in-plane symmetry at the meta-atom level (Figure 4a). We employed the finite-difference time-domain (FDTD) method of the Ansys Lumerical Suite and COMSOL Multiphysics 6.3 simulations (see Note S3) to investigate structural deformation and transmission spectra. The finalized key geometric parameters include P_x = 3.2 μm, P_y = 1.6 μm, d = 0.4 μm, w = 0.8 μm, l_1 = 1.2 μm and l_2 = 1.2 μm, patterned on

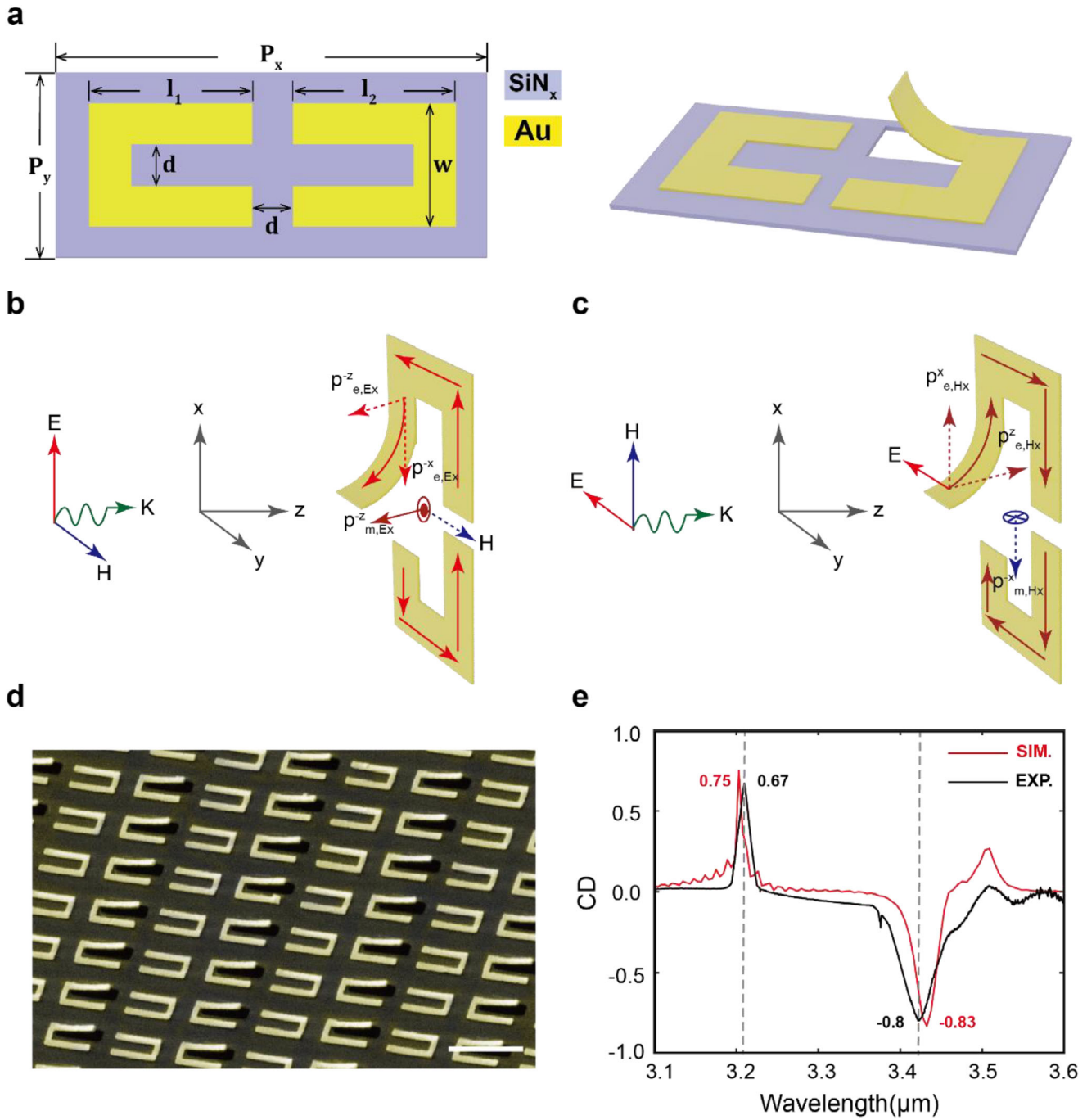

FIGURE 4 | Fabrication and performance of a chiral 3D bending metasurface. (a) Schematic of the unit cell in planar and bent states, featuring two symmetric SRRs with one designated end uplifted post-folding. (b, c) The electromagnetic response of asymmetric 3D SRRs to plane-wave excitation. (d) SEM image of the fabricated 3D chiral metasurface after IBE-induced uniform bending, showing excellent structural uniformity. (e) Measured (black) and simulated (red) CD spectra of the metasurface, showing an experimental giant CD value of 0.8 at 3.41 μm. Scale bar is 2 μm in (d).

a bilayer of 50 nm-thick SiN_x and 50 nm-thick Au. IBE was used to uniformly transform the planar SRR arrays into the designed 3D bending structure. The resulting metasurface exhibited excellent uniformity, as shown in the SEM image in Figure 4d (Figure S9b for large scale). Next, we separately explain how this 3D structure achieves chiral selection through the electric (Figure 4b) and magnetic (Figure 4c) response components excited by the electromagnetic field [40]. An x-directed electric field induces an x- directed electric dipole moment in the planar part of the asymmetric SRRs, denoted as p^{x}_{e,E_x}. The resultant electric dipole moment generated in the uplifted segment can be decomposed into two components: p^{-x}_{e,E_x} and p^{-z}_{e,E_x}. The currents associated with these electric dipole moments further generate a z-directed magnetic dipole moment in the split ring, p^{-z}_{m,E_x}. Moreover, an x-directed magnetic field excitation induces an x-directed magnetic dipole moment p^{-x}_{m,H_x} in the planar part. From current continuity, the corresponding electric dipole moments in the uplifted segment are p^{x}_{e,H_x} and p^{z}_{e,H_x}. Therefore, along with $p^{-z}_{m,E_x} \perp H$, $p^{x}_{e,H_x} \perp E$ and $p^{z}_{e,H_x} \perp E$, it can be deduced that this structure induces polarization rotation, thereby achieving chiral selection.

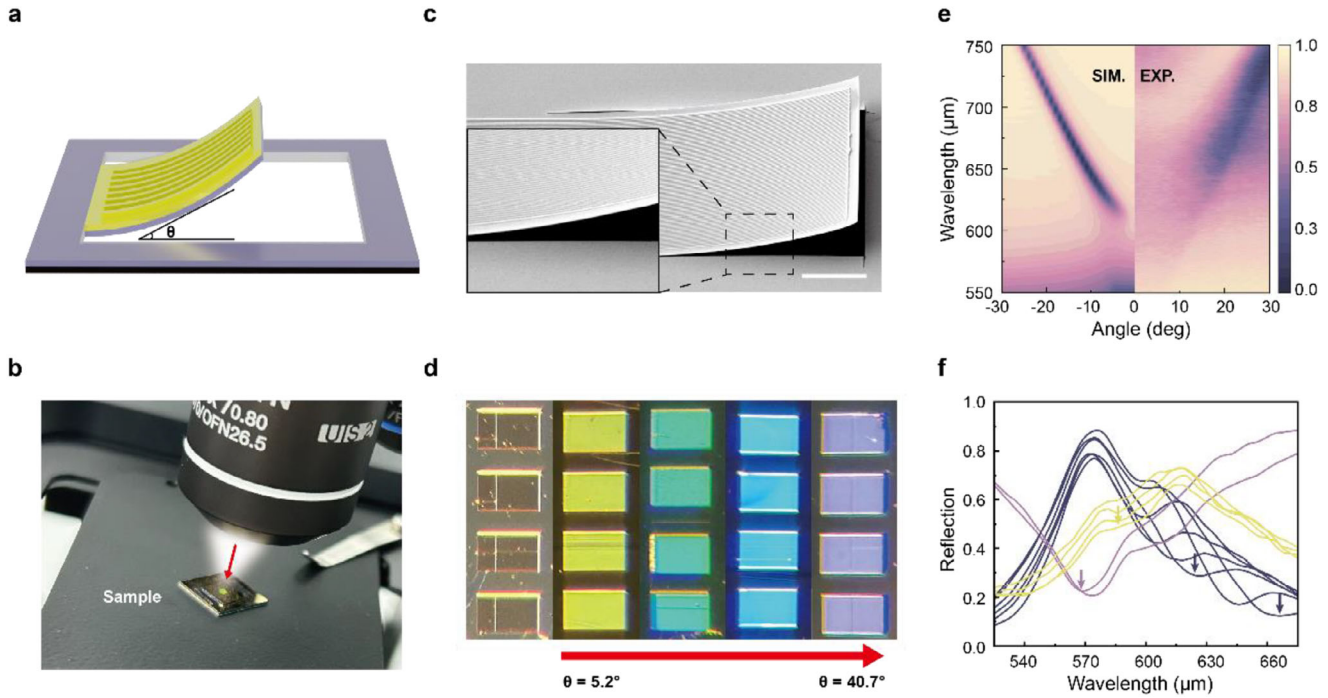

FIGURE 5 | Fabrication and spectral tuning of a collectively buckled plasmonic grating supporting BICs. (a) Schematic of the bent grating denoting the tangential curvature of the grating with θ. (b) Schematic of the experimental setup for observing reflected color variations from gratings with different bending angles under white-light illumination. (c) SEM image of the grating after IBE-induced global buckling. The inset shows a magnified view of the area within the black dashed box. (d) Optical microscopy images of the grating structure under white-light exposure, demonstrating a progressive blue shift in reflected color with increasing bending angles. (e) Simulated (left) and experimentally measured (right) angle-resolved reflectance spectra of the planar plasmonic grating structure. (f) Reflectance spectra measured from different positions on the bent grating under oblique incidence conditions. The arrows indicate a 100 nm blueshift of the transmission dip. Scale bar is 20 μm in (c).

Optical characterization confirmed the device's strong chiral properties. The measured CD $= (T_L - T_R)/(T_L + T_R)$ reached a value of 0.8 at 3.41 μm (Figure 4e, black curve), which closely matched the simulated spectrum (red curve). This high CD value demonstrates significant intrinsic chirality, arising from the IBE-fabricated uplifted segment, which creates a non-zero product of electric and magnetic dipole moments under optical excitation. Additionally, applying IBE to bend an initially asymmetric SRR structure produced a similarly high CD value of 0.79 at 3.56 μm (Figure S10), further confirming the method's effectiveness in creating chiral responses.

Beyond inducing local deformation at the meta-atom level, IBE also enables the global and collective deformation of entire device platforms. This capability is demonstrated by a visible-spectrum tunable plasmonic grating. The device started as a one-dimensional planar *Au* grating on a suspended SiN_x membrane, designed to support a symmetry-protected BIC (see Note S5). The planar structure was first characterized and exhibited a resonance near 610 nm (Figure 5e, right), consistent with the 610 nm resonance predicted by simulation (Figure 5e, left).

IBE irradiation was then used to induce controlled global buckling across the entire released grating structure (Figure 5c), creating a stable curved platform. The tuning effect was immediately visible, with the reflected color under white-light illumination shifting towards blue as the bending angle increased (Figure 5d). Quantitative optical measurements performed at different positions on the curved grating (Figure 5a) showed that the BIC resonance could be shifted from approximately 650 nm to 500 nm (Figure S11). The simulation results for the tunable movable grating are presented in (Figure S13). Based on the positional change of the arrow on the reflectance spectra, it can be determined that the resonance dip measured under standardized conditions has undergone a net blue shift of 100 nm (Figure 5f), validating the dynamic spectral tuning capability of the IBE-buckled grating in the visible range.

These two demonstrations highlight the versatile application of IBE in photonics. The technology enables the precise fabrication of local 3D features for functional devices like chiral metasurfaces, and also facilitates the global reconfiguration of device platforms for active optical tuning. This ability to program 3D geometry across scales makes IBE a key technology for the development of advanced and dynamic optical devices.

3 | Discussion

The IBE-induced reshaping technology presented here demonstrates distinct advantages within the landscape of 3D nanofabrication techniques. As summarized in Table 1, broad-beam IBE uniquely integrates genuine wafer-scale parallel processing with sub-10-nm feature control. While capillary force origami can achieve high throughput, its stochastic nature limits geometric precision and angular control. Compression buckling depends heavily on specific material mechanics and complicates integration with standard fabrication. Residual stress-induced methods

TABLE 1 | Summary of key characteristic metrics of various 3D folding methods with their disadvantages. The asterisk (*) **indicates** "this work".

Fabrication method	Area size	Time	Uniformity	Feature size
Ion beam etching induced bending *	~4 inch	10–20 s	Over 95%	Sub 10 nm
Capillary force origami [28–30]	~100 μm	~80 s	Decrease rapidly with spacing	Sub micro
Compression buckling [22–24]	~60 μm	~60 s	80 – 88%	~ micro
Residual stress-induced bending [9, 26]	A hundred-micrometer scale	~50 s	Above 80%	Sub micro
Focused ion beam induced folding [32, 33]	~100 μm	3~7 min (increases rapidly with size)	Over 90%	Sub 10 nm

demand stringent control over thin-film stress and lack broad versatility. Most notably, although serial FIB offers excellent positioning accuracy, its sequential nature introduces directional artifacts and non-uniform stress distributions, fundamentally limiting scalability and uniformity for large-area or symmetric structures. In contrast, the parallel, uniform implantation of IBE directly addresses the critical scaling challenge in 3D photonics. It provides deterministic control over 3D geometry, compatibility with standard planar nanofabrication workflows, and material generality. This combination effectively bridges the persistent gap between complex 3D design and scalable manufacturing.

In summary, we have demonstrated a wafer-scale 3D nanofabrication platform using parallel broad-beam IBE. This technique enables the rapid, uniform transformation of 2D patterns into precise 3D geometries across entire substrates, overcoming the critical throughput-precision trade-off. The process achieves exceptional angular uniformity (>97%) and reduces fabrication time by over two orders of magnitude compared to serial methods. The platform's versatility is proven by fabricating two functional devices: a chiral 3D bending metasurface with an experimental giant CD of ~ 0.8 in the mid-infrared, and a tunable plasmonic grating with > 150 nm resonance shift in the visible spectrum. By uniquely combining nanoscale precision with parallel manufacturing, this work bridges the gap between complex 3D design and scalable production, offering a robust pathway for next-generation integrated photonics.

However, IBE also has limitations, such as a lack of programmability, limited spatial selectivity, and the inability to achieve site-specific dose control. Nevertheless, we have proposed several effective solutions. By using a physical stencil mask, IBE can perform selective ion irradiation, where the unmasked areas receive irradiation while the masked regions remain planar. With the assistance of FIB, EBL, or UV lithography, sub-micrometer-resolution masks can be fabricated [53–56], which not only enable site-specific dose control but also allow cross-scale fabrication from nanometers to millimeters. Moreover, because the IBE chamber is sufficiently large, multiple stacked masks can be employed to realize dose control in different areas. Once the masks are fabricated, the parallel processing nature of IBE allows for high-throughput fabrication of large batches of samples.

4 | Methods

4.1 | Broad-Beam IBE Process

Patterned membranes were carefully placed into the high-vacuum chamber of a commercial IBE system equipped with a Kaufman-type argon ion source and advanced beam focusing optics. Transformation of 2D planar patterns into 3D architectures was accomplished via direct broad-beam irradiation under precisely controlled conditions. Critical parameters including irradiation time, ion beam current density, and incident angle were selectively modulated according to specific design requirements to construct various 3D configurations with tailored geometrical properties. The base pressure was maintained below 1×10^{-4} Torr throughout all experiments to ensure process purity and reproducibility.

4.2 | Sample Fabrication

A 50 nm-thick low-stress silicon nitride membrane with excellent mechanical stability was utilized as the primary substrate throughout this study. For infrared-responsive metasurface fabrication, the fabrication process has been described in detail (see Note S1). The fabrication process of the tunable visible grating structures is detailed in Note S5. Selective dry etching in an advanced reactive ion etching system with endpoint detection was employed where necessary to completely remove exposed silicon nitride regions without affecting protected areas.

4.3 | Numerical Simulation

Theoretical analysis of metasurface optical responses was conducted based on the finite element method using commercially available software packages to determine optimal structures and clarify underlying mechanisms of intrinsic chiral optical

response. Full-wave electromagnetic simulations were performed using periodic boundary conditions in the x-y plane with perfectly matched layers implemented along the z-direction to properly terminate light wave propagation and avoid unphysical reflections. Material dispersion was rigorously accounted for using experimentally measured dielectric functions, and structural deformation was simulated using coupled mechanical-electromagnetic models to accurately predict performance of folded configurations.

4.4 | Optical Characterization

More detailed information is described in Note S6.

Acknowledgements

This work was supported by the National Key Research and Development Program of China under Grant Nos. 2024YFA1207700, 2022YFA1204100; National Natural Science Foundation of China under Grants Nos. 92265110, 62174179, 12104133; Strategic Priority Research Program of the Chinese Academy of Sciences under Grant Nos. XDB33020200 and the Open Research Fund of Beijing National Laboratory for Condensed Matter Physics (2024BNLCMPKF014). This work was supported by the Joint Fund Project of the Provincial Science and Technology R&D Program of Henan Province (245200810089), and the Key Research Projects Program for Higher Education Institutions of Henan Province (26A140005). This work was also supported by the Micro/nano Fabrication Laboratory of Synergetic Extreme Condition User Facility (SECUF).

Conflicts of Interest

The authors declare no conflicts of interest.

Data Availability Statement

The data that support the findings of this study are available from the corresponding author upon reasonable request.

References

1. Y. Yang, Y. Jeon, Z. Dong, et al., "Nanofabrication for Nanophotonics," *ACS Nano* 19 (2025): 12491–12605, https://doi.org/10.1021/acsnano.4c10964.

2. C. M. Soukoulis and M. Wegener, "Past Achievements and Future Challenges in the Development of Three-Dimensional Photonic Metamaterials," *Nature Photonics* 5 (2011): 523–530, https://doi.org/10.1038/nphoton.2011.154.

3. Y. Zhang, F. Zhang, Z. Yan, et al., "Printing, Folding and Assembly Methods for Forming 3D Mesostructures in Advanced Materials," *Nature Reviews Materials* 2 (2017): 17019, https://doi.org/10.1038/natrevmats.2017.19.

4. H. Chen, X.-L. Zhang, Y.-Y. Zhang, et al., "Atomically Precise, Custom-Design Origami Graphene Nanostructures," *Science* 365 (2019): 1036–1040, https://doi.org/10.1126/science.aax7864.

5. G. P. Collins, "Kirigami and Technology Cut a Fine Figure, Together," *Proceedings of the National Academy of Sciences* 113 (2016): 240–241, https://doi.org/10.1073/pnas.1523311113.

6. J. J. Park, P. Won, and S. H. Ko, "A Review on Hierarchical Origami and Kirigami Structure for Engineering Applications," *International Journal of Precision Engineering and Manufacturing-Green Technology* 6 (2019): 147–161, https://doi.org/10.1007/s40684-019-00027-2.

7. Z. Liu, A. Cui, J. Li, and C. Gu, "Folding 2D Structures Into 3D Configurations at the Micro/Nanoscale: Principles, Techniques, and Applications," *Advanced Materials* 31 (2019): 1802211, https://doi.org/10.1002/adma.201802211.

8. S. Hu, C. Park, and S. Jeong, "Additive Manufacturing of Metastructures at the Micro- and Nano-Scale," *Chemical Society Reviews* 55 (2026): 1666–1716, https://doi.org/10.1039/D4CS01054J.

9. C. C. Chen, C. T. Hsiao, S. Sun, et al., "Fabrication of Three Dimensional Split Ring Resonators by Stress-Driven Assembly Method," *Optics Express* 20 (2012): 9415, https://doi.org/10.1364/OE.20.009415.

10. S. Chen, J. Chen, X. Zhang, J. Li, and J. Li, "Kirigami/Origami: Unfolding the New Regime of Advanced 3D Microfabrication/Nanofabrication With "Folding"," *Light: Science & Applications* 9 (2020): 75, https://doi.org/10.1038/s41377-020-0309-9.

11. F. Feng, P. Plucinsky, and R. D. James, "Helical Miura Origami," *Physical Review E* 101 (2020): 033002, https://doi.org/10.1103/PhysRevE.101.033002.

12. R. Pan, Z. Liu, W. Zhu, S. Du, C. Gu, and J. Li, "Asymmetrical Chirality in 3D Bended Metasurface," *Advanced Functional Materials* 31 (2021): 2100689, https://doi.org/10.1002/adfm.202100689.

13. T. Kan, A. Isozaki, N. Kanda, et al., "Enantiomeric Switching of Chiral Metamaterial for Terahertz Polarization Modulation Employing Vertically Deformable MEMS Spirals," *Nature Communications* 6 (2015): 8422, https://doi.org/10.1038/ncomms9422.

14. J. Binysh, T. R. Wilks, and A. Souslov, "Active Elastocapillarity in Soft Solids With Negative Surface Tension," *Science Advances* 8 (2022): abk3079, https://doi.org/10.1126/sciadv.abk3079.

15. H. T. Lee, S. Lee, J. Kim, H. J. Shin, H. R. Park, and J. Rho, "3D-Printed Mechanically Reconfigurable All-Dielectric Metagrating for Terahertz Filters," *Journal of Applied Physics* 139 (2026): 093101, https://doi.org/10.1063/5.0309175.

16. D. Han, W. Li, T. Sun, et al., "2D-to-3D Buckling Transformability Enabled Reconfigurable Metamaterials for Tunable Chirality and Focusing Effect," *Photonics Research* 11 (2023): 1770, https://doi.org/10.1364/PRJ.500751.

17. W. Jung, Y.-H. Jung, P. V. Pikhitsa, et al., "Three-Dimensional Nanoprinting Via Charged Aerosol Jets," *Nature* 592 (2021): 54–59, https://doi.org/10.1038/s41586-021-03353-1.

18. G. Yoon, I. Kim, S. So, J. Mun, M. Kim, and J. Rho, "Fabrication of Three-Dimensional Suspended, Interlayered and Hierarchical Nanostructures by Accuracy-Improved Electron Beam Lithography Overlay," *Scientific Reports* 7 (2017): 6668, https://doi.org/10.1038/s41598-017-06833-5.

19. C. Wang, Z. Li, R. Pan, et al., "Giant Intrinsic Chirality in Curled Metasurfaces," *ACS Photonics* 7 (2020): 3415–3422, https://doi.org/10.1021/acsphotonics.0c01230.

20. R. Pan, S. Du, Z. Liu, C. Gu, and J. Li, "3D Cross-Bended Metasurfaces With Polarization Insensitivity and High-Q Resonances," *Journal of Optics* 22 (2020): 105103, https://doi.org/10.1088/2040-8986/abad51.

21. X. Hong, Q. Liang, X. Liu, C.-Y. Ji, and J. Li, "Manipulation of Fractal Nano-Kirigami by Capillary and Electrostatic Forces," *Advanced Optical Materials* 11 (2023): 2202150, https://doi.org/10.1002/adom.202202150.

22. Y. Yang, W. Jung, C. Hur, et al., "Angle-Resolved Polarimetry With Quasi-Bound States in the Continuum Plasmonic Metamaterials via 3D Aerosol Nanoprinting," *ACS Nano* 18 (2024): 12771–12780, https://doi.org/10.1021/acsnano.3c12024.

23. J.-L. Yang, Q.-C. Yuan, R.-F. Chen, et al., "Enhanced Third-Harmonic Generation in Silicon Metasurface," *Acta Physica Sinica* 68 (2019): 214207, https://doi.org/10.7498/aps.68.20190789.

24. M. E. Reimer, G. Bulgarini, N. Akopian, et al., "Bright Single-Photon Sources in Bottom-Up Tailored Nanowires," *Nature Communications* 3 (2012): 737, https://doi.org/10.1038/ncomms1746.

25. J.-H. Park, A. Ndao, W. Cai, et al., "Symmetry-Breaking-Induced Plasmonic Exceptional Points and Nanoscale Sensing," *Nature Physics* 16 (2020): 462–468, https://doi.org/10.1038/s41567-020-0796-x.

26. S. Hu, Y. Li, B. Dong, et al., "Highly Hydrostable and Flexible Opal Photonic Crystal Film for Enhanced Up-Conversion Fluorescence Sensor of COVID-19 Antibody," *Biosensors and Bioelectronics* 237 (2023): 115484, https://doi.org/10.1016/j.bios.2023.115484.

27. Z. M. Yu, K. Zhao, L. Li, C. Ye, Y. Dong, and Y. Song, "A Vivid Au-Porous Anodic Alumina Composite Film With the Inverted Taper Structure for Label-Free Detection," *Nano Research* 16 (2023): 9997–10003, https://doi.org/10.1007/s12274-023-5549-6.

28. S. Xu, Z. Yan, K.-I. Jang, et al., "Assembly of Micro/Nanomaterials Into Complex, Three-Dimensional Architectures by Compressive Buckling," *Science* 347 (2015): 154–159, https://doi.org/10.1126/science.1260960.

29. W. Liu, Q. Zou, C. Zheng, and C. Jin, "Metal-Assisted Transfer Strategy for Construction of 2D and 3D Nanostructures on an Elastic Substrate," *ACS Nano* 13 (2019): 440–448, https://doi.org/10.1021/acsnano.8b06623.

30. H.-S. Ee and R. Agarwal, "Tunable Metasurface and Flat Optical Zoom Lens on a Stretchable Substrate," *Nano Letters* 16 (2016): 2818–2823, https://doi.org/10.1021/acs.nanolett.6b00618.

31. P. Gutruf, C. Zou, W. Withayachumnankul, M. Bhaskaran, S. Sriram, and C. Fumeaux, "Mechanically Tunable Dielectric Resonator Metasurfaces at Visible Frequencies," *ACS Nano* 10 (2016): 133–141, https://doi.org/10.1021/acsnano.5b05954.

32. Z. Tian, B. Xu, B. Hsu, L. Stan, Z. Yang, and Y. Mei, "Reconfigurable Vanadium Dioxide Nanomembranes and Microtubes With Controllable Phase Transition Temperatures," *Nano Letters* 2018, 18, 3017–3023, https://doi.org/10.1021/acs.nanolett.8b00483.

33. W. Huang, S. Koric, X. Yu, K. J. Hsia, and X. Li, "Precision Structural Engineering of Self-Rolled-up 3D Nanomembranes Guided by Transient Quasi-Static FEM Modeling," *Nano Letters* 14 (2014): 6293–6297, https://doi.org/10.1021/nl5026369.

34. F. Iker, N. André, T. Pardoen, and J.-P. Raskin, "One-Mask CMOS Compatible Process for the Fabrication of Three-Dimensional Self-Assembled Thin-Film SOI Microelectromechanical Systems," *Electrochemical and Solid-State Letters* 8 (2005): H87, https://doi.org/10.1149/1.2030488.

35. C. Py, P. Reverdy, L. Doppler, J. Bico, B. Roman, and C. Baroud, "Capillary Origami," *Physics of Fluids* 19 (2007): 091104, https://doi.org/10.1063/1.2775288.

36. Z. Lao, Y. Hu, C. Zhang, et al., "Capillary Force Driven Self-Assembly of Anisotropic Hierarchical Structures Prepared by Femtosecond Laser 3D Printing and Their Applications in Crystallizing Microparticles," *ACS Nano* 9 (2015): 12060–12069, https://doi.org/10.1021/acsnano.5b04914.

37. X. Lyu, Z. Zheng, A. Shiva, et al., "Capillary Trapping of Various Nanomaterials on Additively Manufactured Scaffolds for 3D Micro-/Nanofabrication," *Nature Communications* 15 (2024): 6693, https://doi.org/10.1038/s41467-024-51086-2.

38. I. Kim, J. Mun, W. Hwang, Y. Yang, and J. Rho, "Capillary-Force-Induced Collapse Lithography for Controlled Plasmonic Nanogap Structures," *Microsystems & Nanoengineering* 6 (2020): 65, https://doi.org/10.1038/s41378-020-0177-8.

39. X. Hong, H. Sun, F. Meng, et al., "Synthetic Nano-Kirigami With High Deformability for Reconfigurable Information Displays," *Nature Communications* 16 (2025): 7843, https://doi.org/10.1038/s41467-025-63169-9.

40. K. Höflich, G. Hobler, F. I. Allen, et al., "Roadmap for Focused Ion Beam Technologies," *Applied Physics Reviews* 10 (2023): 041311, https://doi.org/10.1063/5.0162597.

41. P. J. W. Moll, "Focused Ion Beam Microstructuring of Quantum Matter," *Annual Review of Condensed Matter Physics* 9 (2018): 147–162, https://doi.org/10.1146/annurev-conmatphys-033117-054021.

42. K. Chalapat, N. Chekurov, H. Jiang, J. Li, B. Parviz, and G. S. Paraoanu, "Self-Organized Origami Structures via Ion-Induced Plastic Strain," *Advanced Materials* 25 (2013): 91–95, https://doi.org/10.1002/adma.201202549.

43. P. Zilio, M. Malerba, A. Toma, R. P. Zaccaria, A. Jacassi, and F. D. Angelis, "Hybridization in Three Dimensions: A Novel Route Toward Plasmonic Metamolecules," *Nano Letters* 15 (2015): 5200–5207, https://doi.org/10.1021/acs.nanolett.5b01437.

44. J.-S. Huang, V. Callegari, P. Geisler, et al., "Atomically Flat Single-Crystalline Gold Nanostructures for Plasmonic Nanocircuitry," *Nature Communications* 1 (2010): 150, https://doi.org/10.1038/ncomms1143.

45. C. Ropers, C. C. Neacsu, T. Elsaesser, M. Albrecht, M. B. Raschke, and C. Lienau, "Grating-Coupling of Surface Plasmons Onto Metallic Tips: A Nanoconfined Light Source," *Nano Letters* 7 (2007): 2784–2788, https://doi.org/10.1021/nl071340m.

46. M. Hentschel, K. Koshelev, F. Sterl, et al., "Dielectric Mie voids: Confining Light in Air," *Light: Science & Applications* 12 (2023): 3, https://doi.org/10.1038/s41377-022-01015-z.

47. R. Zheng, R. Pan, C. Sun, et al., "Bidirectional Origami Inspiring Versatile 3D Metasurface," *Advanced Materials Technologies* 7, no. 8 (2022): 2200373.

48. R. Pan, Z. Li, Z. Liu, et al., "Rapid Bending Origami in Micro/Nanoscale Toward a Versatile 3D Metasurface," *Laser & Photonics Reviews* 14 (2019): 1900179, https://doi.org/10.1002/lpor.201900179.

49. Y. H. Lee, Y. Won, J. Mun, et al., "Hierarchically Manufactured Chiral Plasmonic Nanostructures With Gigantic Chirality for Polarized Emission and Information Encryption," *Nature Communications* 14 (2023): 7298, https://doi.org/10.1038/s41467-023-43112-6.

50. S. Hussain, Q. Liu, Z. Maroof, R. Ji, and S. Wang, "Ultra-Broadband and High-Efficiency Planar Chiral Metamaterial," *Optics Letters* 47 (2022): 5700, https://doi.org/10.1364/OL.474003.

51. W. Choi, W. P. Moestopo, S. Gu, et al., "Helical Photonic Metamaterials for Encrypted Chiral Holograms," *Advanced Science* 12 (2025): 07931, https://doi.org/10.1002/advs.202507931.

52. C. Caloz and A. Sihvola, "Electromagnetic Chirality, Part 1: The Microscopic Perspective [Electromagnetic Perspectives]," *IEEE Antennas and Propagation Magazine* 62 (2020): 58–71.

53. P. Weber, E. Guibert, S. Mikhailov, J. Brügger, and G. Villanueva, *AIP Conference Proceedings* 1099 (2009): 539, https://doi.org/10.1063/1.3120093.

54. A. Singh, A. Shi, and S. A. Claridge, "Nanometer-Scale Patterning of Hard and Soft Interfaces: From Photolithography to Molecular-Scale Design," *Chemical Communications* 58 (2022): 13059–13070, https://doi.org/10.1039/D2CC05221K.

55. C. Chia, B. Machielse, A. Shams-Ansari, and M. Lončar, "Development of Hard Masks for Reactive Ion Beam Angled Etching of Diamond," *Optics Express* 30 (2022): 14189, https://doi.org/10.1364/OE.452826.

56. H. Zamani, S. W. Lee, A. Avishai, C. A. Zorman, R. M. Sankaran, and P. X. L. Feng, "Focused Ion-Beam (FIB) Nanomachining of Silicon Carbide (SiC) Stencil Masks for Nanoscale Patterning," *Materials Science Forum* 717–720 (2012): 889–892, https://doi.org/10.4028/www.scientific.net/MSF.717-720.889.

Supporting Information

Additional supporting information can be found online in the Supporting Information section.

Supporting File: adma73929-sup-0001-SuppMat.docx.